



Journal of Mining and Environment (JME)

journal homepage: www.jme.shahroodut.ac.ir



Delineation of Iron Alteration Zones using Spectrum-Area Fractal Model and TOPSIS Decision-Making Method in Tarom Metallogenic Zone, NW Iran

Mohammad Mahdi Pourgholam¹, Peyman Afzal^{1*}, Ahmad Adib¹, Kambiz Rahbar², Mehran Gholinejad¹

1- Department of Petroleum and Mining Engineering, South Tehran Branch, Islamic Azad University, Tehran, Iran

2- Department of Computer Engineering, South Tehran Branch, Islamic Azad University, Tehran, Iran

Article Info

Received 22 March 2022

Received in Revised form 11 June 2022

Accepted 27 June 2022

Published online 27 June 2022

DOI:10.22044/jme.2022.11770.2168

Keywords

Spectrum-Area fractal model

Landsat 8 OLI

TOPSIS

Iron alteration zones

Tarom

Abstract

Signal analysis approaches are a powerful and widely used tool in processing multi-spectral satellite images for detection of alteration zones. The main goal of this work is application of the spectrum-area fractal methodology based on the Landsat 8 OLI satellite images' data for separation alteration zones for iron oxides at the Tarom region (NW Iran). These alteration zones, Normalized Difference Vegetation Index (NDVI), and Normalized Difference Water Index (NDWI) are detected using the band-ratio and band combination methods. Then the calculated values are categorized by Spectral Angle Mapper (SAM), k-means, and S-A fractal model. Considering a positive correlation of iron oxides alterations along with magnetite mineralization as an index of mineralization at the studied region, the promising areas are classified by a decision-making model using the TOPSIS method with an acceptable accuracy for presenting in the exploration models.

1. Introduction

Satellite imagery is a widely used tool, and also as an effective parameter for the mineral exploration operation. Satellite images such as Landsat sensor images provide an efficient tool to use different techniques and methods on the basis of combination of materials on the ground, and the light absorption or reflection frequency reveal the exploration target areas [1-13]. In this research work, in order to achieve acceptable results for presentation in an exploratory model in the subsequent studies, the Landsat OLI 8 satellite data related to the studied area, e.g. the Tarom region, is used. The exploratory model is planned for optimally identifying iron prospects. The major alteration zone is iron oxides/hydroxides. However, considering the local geological conditions, considering the existence of dominant

intrusive masses in the region, to recognize the main mineralization in the region and also evidence of their relationship with iron mineralization ores, aluminous and propylitic ultrasonics are examined. An initial correction on the Landsat OLI 8 data is performed based on the band-ratio and band composition techniques. Next, the iron oxide alteration zones are detected and compared with surface evidence of magnetite mineralization. Then the output images for these detection techniques are classified by the spectrum-area technique, according to the intensity and weakness factors of the alterations, and the classification is presented to the expansion model. The ranking and classification of the promising areas are performed by the TOPSIS model.

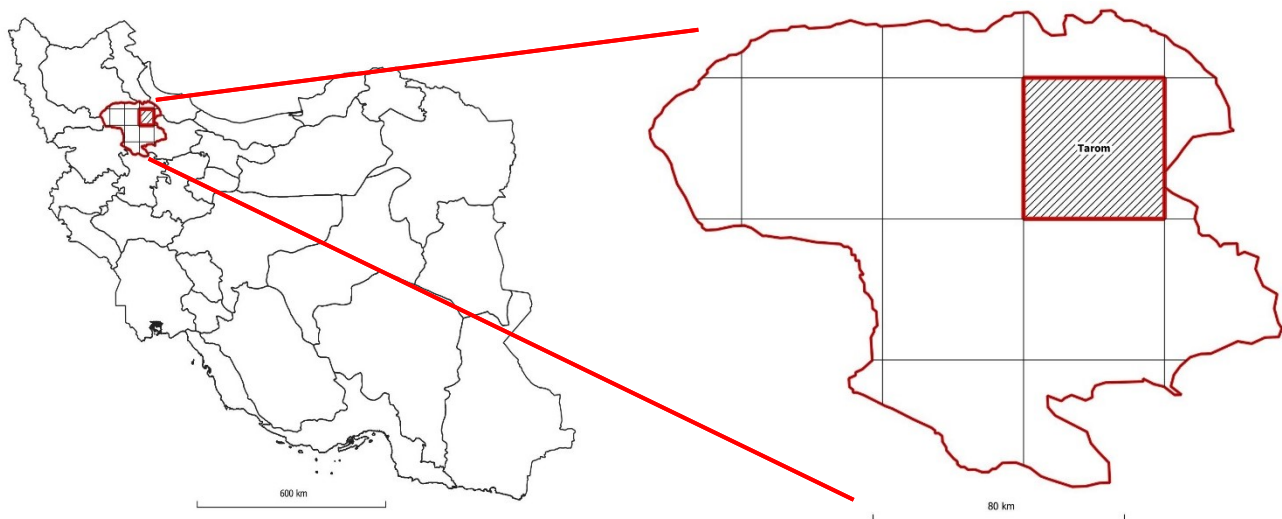
✉ Corresponding author: peymanafzal@gmail.com (P. Afzal).

2. Geological Situation/Setting of Taronm Zone and Materials

2.1. Geological situation/setting of Taronm zone

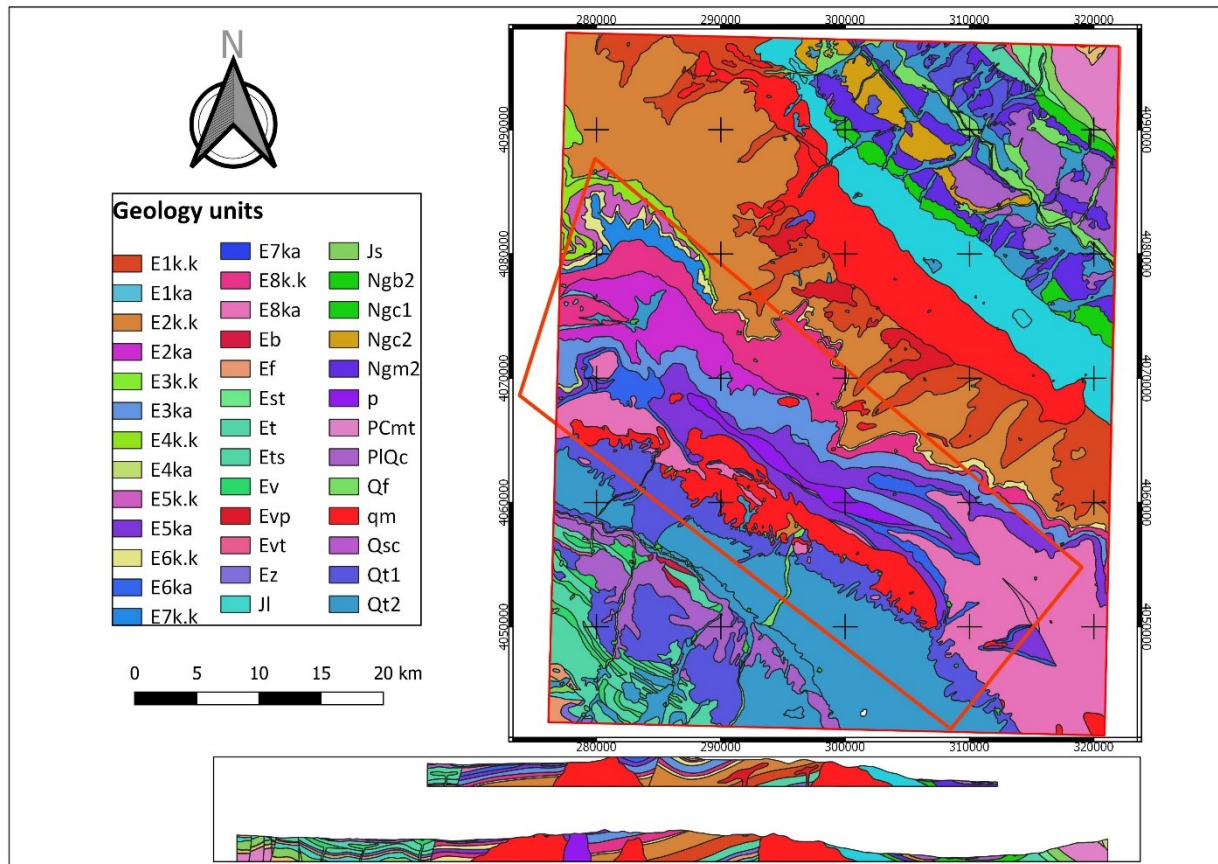
The Taronm district is part of the Zanjan province (NW Iran) that is a part of the Taronm-Hashtjin metallogenic belt by a NW-SE trend (Figure 1). The outcrops of this region are mostly Tertiary intrusive and volcanic rocks. However, the Taronm region is considered as a part of the Central Alborz zone in the geological structural division of Iran [14]. This mountain range is associated of layers as pyroclastic and volcanic rocks. Most rock types are of andesitic and rhyolite rocks, with low volumes of basaltic units. Eocene volcanic eruption has a variety of trachite-trachyandesite, and lapili tuff pyroclastic rocks. Furthermore, intrusives consist of Late Eocene-Oligocene quartz monzonite, monzonite, and granite. There is much metallic mineralization including Cu-Au, Fe, Pb-Zn, and Fe-P-REE mineralization [4 &15].

In this area, Eocene volcanic masses were intruded by a 3–5 km wide and 10–15 km long NW-SE trending intrusions of Upper Eocene quartz-monzonites to quartz-monzodiorites and monzogranites, as shown in Figure 1 [12]. The plutonic bodies are metaluminous I-type granitoid, and have calc-alkaline affinity[10]. There are iron oxide-apatite (IOA) ores including Sorkheh-Dizaj, Aliabad, Morvarid, Zaker, Golestan Abad, Zarnan, and Chorehnab. These deposits are hosted by quartz-monzonites, volcanic, and volcanoclastic rocks [15, 17&18]. Mineralogically, these IOA deposits are composed of magnetite, apatite, monazite, actinolite, clinopyroxene, pyrite, chalcopyrite, quartz, and calcite. One of the most important pieces of evidence of this type of mineralization is iron composites including Fe^{+3} , Fe^{+2} and magnetite forms of mineralization as an endmember to detect in the studied area. Also all other types of Fe mineralization that may have a relation to the IOA type of mineralization are considered to indicate the exploration factors.



(a)

Figure 1. A. Taronm 1:100000 sheet position. B. Geological setting of Taronm 1:100000 sheet. C. Important Geological units.



(b)

- E1k.k, Greenish gray tuffaceous sandstone, tuff, mudstone.
- E2k.k, Tuff, tuffaceous sandstone, siltstone, mudstone with intercalation of tuff.
- E3k.a, Sandstone with intercalated mudstone.
- E6k.k, Light green to pink tuff breccia, lapilli tuff, pumice tuff, welded tuff, crystal lithic tuff.
- Ngc1, Red conglomerate.
- Ngm2, Alternation of light green gypsiferous marl, gypsum with reddish gray clay, sandstone and conglomerate.
- Qt2, Young terraces.
- qm, Quartz monozodiorite - quartz monzonite, quartz syenite.

(c)

Continuos of Figure 2. A. Tarom 1:100000 sheet position. B. Geological setting of Tarom 1:100000 sheet. C. Important Geological units.

2.2. Materials

2.2.1. Multi-spectral image's data

A cloud-free level 1T entitled as terrain corrected of Landsat 8 satellite with OLI sensor with path and row 166 and 35, respectively, was derived via the U.S. Geological Survey Earth Resources Observation and Science Center [20].

The Operational Land Imager (OLI) spectral bands prepare improvement from prior Landsat

tools, with the additional two developed spectral bands consisting of 1) a deep blue visible band for water resources and coastal zone identification; and 2) an innovative infrared band (9) for the recognition of cirrus clouds. Two thermal bands as named TIRS detection data with a 100 m minimum resolution but they are recorded and delivered with the 30 m OLI data. The Landsat 8 file sizes are larger than the Landsat 7 data due to additional bands and improved 16-bit data product [20].

Table 1. Processing and L1T terrain correction parameters.

Processing	Level 1T/Terrain correction
Pixel size (m)	<ul style="list-style-type: none"> • OLI Multispectral bands = 30 • OLI panchromatic band = 15 • TIRS = 100 that is resampled to 30 m to match the OLI multi-spectral bands
Data characteristics	<ul style="list-style-type: none"> • GeoTIFF data format • Cubic convolution (CC) resampling • North up (MAP) orientation • Universal transverse mercator (UTM) map projection (polar stereographic for antarctica) • World geodetic system (WGS) 84 datum • 12 m circular error, 90% confidence global accuracy for OLI • 41 m circular error, 90% confidence global accuracy for TIRS • 16-bit pixel values

The Landsat 8 OLI Level 1T data has a wide variety of corrections on its raw data using ordinary modification procedures for SWIR bands mentioned in Table 1. Thus the Orthorectification & Cross Track Illumination Corrections were done before doing any further processing for better and accurate results [21]. Subsequently, these bands were subjected to atmospheric correction using Fast Line of Sight Atmospheric Analysis Spectral Hypercube entitled as FLAASH [22]. An atmospheric improvement was done using the FLAASH algorithm on the Landsat 8 OLI L1 data related to the Tarom area (Figure 2). All data from

Landsat 8 bands were layer stacked, and the central wavelength values were allocated to related bands for further analysis.

2.2.2. Spectral features of iron minerals

The alteration zones occur in a variety of geological features specifically volcano plutonic units with index mineral alterations as an exploration key. The iron alteration zones usually consist of limonite, hematite, goethite, and Jarosite. A rock’s reflectance spectrum is related to its mineralogical composition.

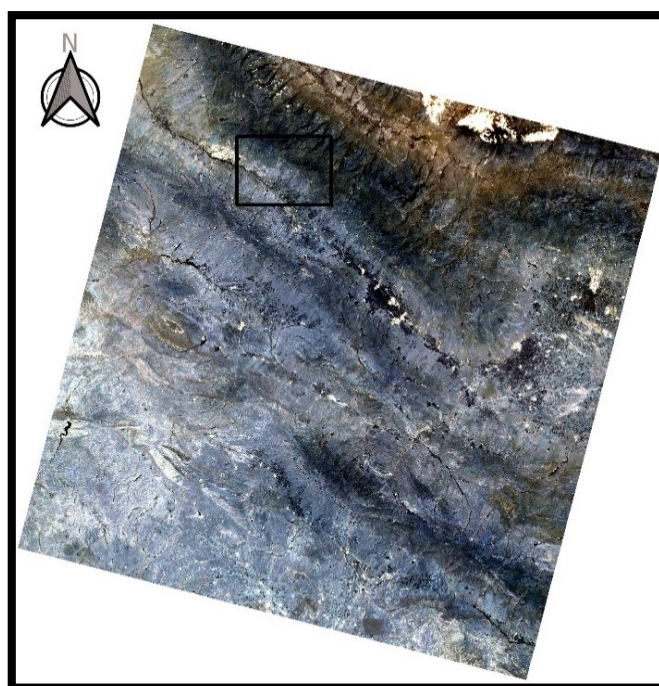


Figure 3. An overview of Tarom region from The Landsat 8 OLI, atmospheric correction done using FLAASH algorithm (RGB:257).

Table 2. Band designations in different sensors 0.

Band designations	Landsat band wavelength comparisons									
	All bands 30-meter resolution unless noted									
	L8 OLI/TIRS		L7 ETM+		L4-5 TM		L4-5 MSS*		L1-3 MSS*	
Coastal/Aerosol	Band 1	0.43–0.45	--	--	--	--	--	--	--	--
Blue	Band 2	0.45–0.51	Band 1	0.45–0.52	Band 1	0.45–0.52	--	--	--	--
Green	Band 3	0.53–0.59	Band 2	0.52–0.60	Band 2	0.52–0.60	Band 1	0.5–0.6 *	Band 4	0.5–0.6 *
Panchromatic	Band 8**	0.50–0.68	Band 8 **	0.52–0.90	--	--	--	--	--	--
Red	Band 4	0.64–0.67	Band 3	0.63–0.69	Band 3	0.63–0.69	Band 2	0.6–0.7 *	Band 5	0.6–0.7 *
Near-Infrared	Band 5	0.85–0.88	Band 4	0.77–0.90	Band 4	0.76–0.90	Band 3	0.7–0.8 *	Band 6	0.7–0.8 *
Near-Infrared	--	--	--	--	--	--	Band 4	0.8–1.1 *	Band 7	0.8–1.1*
Cirrus	Band 9	1.36–1.38	--	--	--	--	* Acquired at 79 m, resampled to 60 m			
Shortwave Infrared-1	Band 6	1.57–1.65	Band 5	1.55–1.75	Band 5	1.55–1.75	** 15-m (panchromatic)			
Shortwave Infrared-2	Band 7	2.11–2.29	Band 7	2.09–2.35	Band 7	2.08–2.35	T1 = Thermal (acquired at 100 m, resampled to 30 m)			
Thermal	Band 10 T1	10.60–11.19	Band 6 T2	10.40–12.50	Band 6 T2	10.40–12.50	T2 = Thermal (acquired at 120 m, resampled to 30 m)			
Thermal	Band 11 T1	11.50–12.51	--	--	--	--				

Table 3. Bands of each Landsat satellite and descriptions of how each band is best used 0.

Band name	Uses of Landsat bands					Description of use
	L8 OLI/TIRS	L7 ETM+	L4-5 TM	L4-5 MSS	L1-3 MSS	
Coastal/Aerosol	Band 1	--	--	--	--	Coastal areas and shallow water observations; aerosol, dust, smoke detection studies.
Blue (B)	Band 2	Band 1	Band 1	--	--	Bathymetric mapping; soil/vegetation discrimination, forest type mapping, and identifying manmade features.
Green (G)	Band 3	Band 2	Band 2	Band 1	Band 4	Peak vegetation; plant vigor assessments.
Red (R)	Band 4	Band 3	Band 3	Band 2	Band 5	Vegetation type identification; soils and urban features.
Near-Infrared (NIR)	Band 5	Band 4	Band 4	Band 3	Band 6	Vegetation detection and analysis; shoreline mapping and biomass content.
	--	--	--	Band 4	Band 7	
Shortwave Infrared-1 (SWIR-1)	Band 6	Band 5	Band 5	--	--	Vegetation moisture content/drought analysis; burned and fire affected areas; detection of active fires.
Shortwave Infrared-2 (SWIR-2)	Band 7	Band 7	Band 7	--	--	Additional detection of active fires (especially at night); plant moisture/drought analysis.
Panchromatic (PAN)	Band 8	Band 8	--	--	--	Sharpening multispectral imagery to higher resolution.
Cirrus	Band 9	--	--	--	--	Cirrus cloud detection.
Thermal (T)	Band 10 Band 11	Band 6	Band 6	--	--	Ground temperature mapping and soil moisture estimations.

The spectra of the main materials found in this region were derived via the USGS spectral library, as depicted in Figure 3 [23]. The US Geological Survey's spectral library was utilized to study the magnetite mineral spectrum. In the first step, we re-wrote the spectral library due to the Image Bands Center of Landsat 8. Then we extracted the magnetite spectrum (3B HS195 Magnetite) from it. Correspondingly, in the area of the image that ensured the existence of iron ores ae purity above 50% was presented (location of mine dump and granulation plant), we selected a spectrum and analyzed it using the "spectral analysis" method, and it was almost 90% the same as the library spectrum.

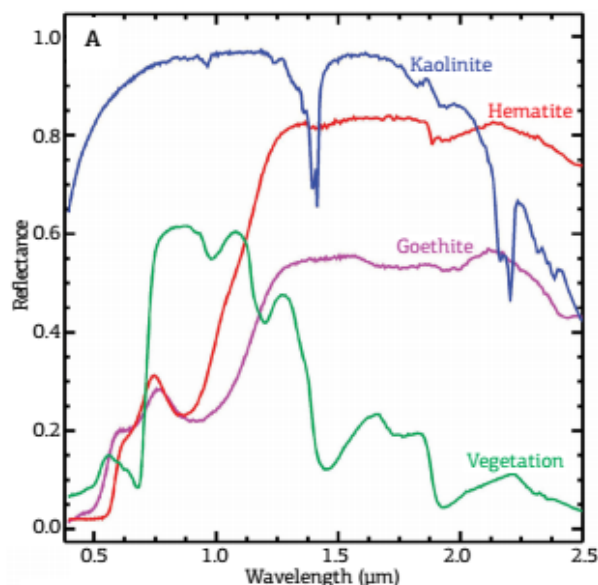


Figure 4. Reflectance spectra from USGS spectral library showing main minerals found on surface of Tarom region.

3. Methodology

3.1. Band ratio

This methodology is practical to suppress topographical difference and brightness variation of images according to the grain sizes' variation [24]. However, this technique has been utilized for mapping geological features, e.g. alteration zones and rock types delineation based on differences between the spectral reflectance properties of rocks and altered [25]. Band ratio can reduce the effect of environmental artifacts. Many studies reveal representative band ratios that are used for enhancing different rocks [1, 6, 26 & 26]. This method includes dividing two bands on each other. The band with the most reflection is placed in the numerator and another band with the most reflection is placed in the denominator. The spectral characteristics of iron index altered minerals, usually are band3/band1 [24]. Van Der Meer [28] has suggested that iron-rich and other associated minerals with hydrothermal processes can be outlined by band4/band2 of Landsat 8 OLI image. According to the band frequency comparison in Table 2, the match bands are band 4 instead of band 3 in TM and band 4 instead of band 1. The results obtained by combining these two ratios are presented in Figure 4. Ali and Pour [29] have suggested a combination of band4/band2, band6/band7, and 5 as RGB for recognition of lithology, altered rocks, and vegetation. Several pairs of bands have offered delineation of various rock-mineral types such as: (Figure 4 a) band4/band2–iron oxide, Figure 4 b) band6/band5– ferrous mineral [3, 30]. The values of band4/band2 and band6/band5 globally show iron oxides in the studied zone.

In this work, several methodologies were applied, and their results were correlated with geological specifics identified from the geological map of the Tarom sheet and other geological data. The iron oxides in the region are hematite, goethite, Jarosite, limonite, and magnetite. Furthermore, band4/band2 and band7/band5 and band7/band2

and band7/band1 are used for extraction of iron oxides. Each ratio shows one feature of an alteration or mineralization. Therefore, the results should be visualized as mono-color images. The band 4/band2 globally shows the iron oxides in the studied region based on the reflectance of Iron mentioned in Tables 1, 2 (Figure 4), and the other ratio related to reflectance and absorption of magnetite needs to be RGB visualized in the band-combination process.

3.2. Band combination

True color images are a result of a mixture of the three primary gray images. False-color images, mostly infra-red images, have certain advantages over true color images. The true color images are often utilized to recognize different geological units, while infra-red images are also highly recognizable [31]. The atmospheric attenuation such as fog, light scattering from clouds can be eliminated [32]. The major benefit of real color images is the accuracy for the detection of rock types. The band compositions such as RGB B7B6B4 or RGB B7B6B4 apply to separate rocks in alteration zones based on the color intensity changes. However, it is hard to extract the bond compounds that illuminate the target unit [33].

3.3. Visual interpretation (Band combination)

The result derived via the approach is mono-color, and needs to be colorized to have a better interpretation with sharpening more details. Based on this method, these components such as vegetation and alteration zones are indicated by a color spectrum. The essential color combination for showing the iron alteration is RGB equal to (4/2,1,1), which displays iron-oxide mineralization in yellow and light green (Figure 5 (B)), and the other ratios related to magnetite mineralization and alteration from band ratio process visualized using the color combination of RGB: (7/5,7/2,7/1; Figure 5 A).

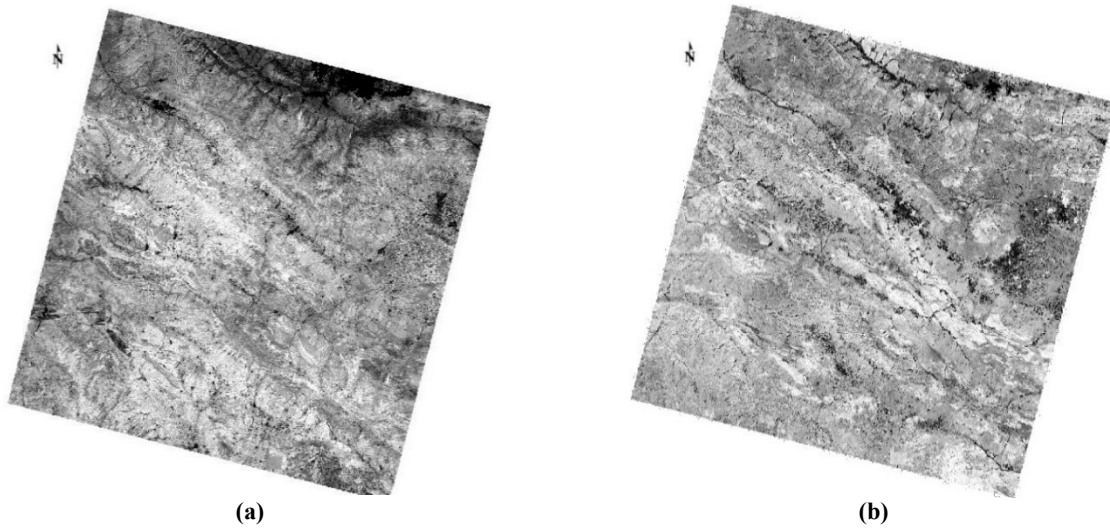


Figure 5. Ratio of band4/band2 and band6/band5 globally shows iron oxides in Tarom zone. A. band4/band2–iron oxide. B. band6/band5 ferrous mineral band6/band5.

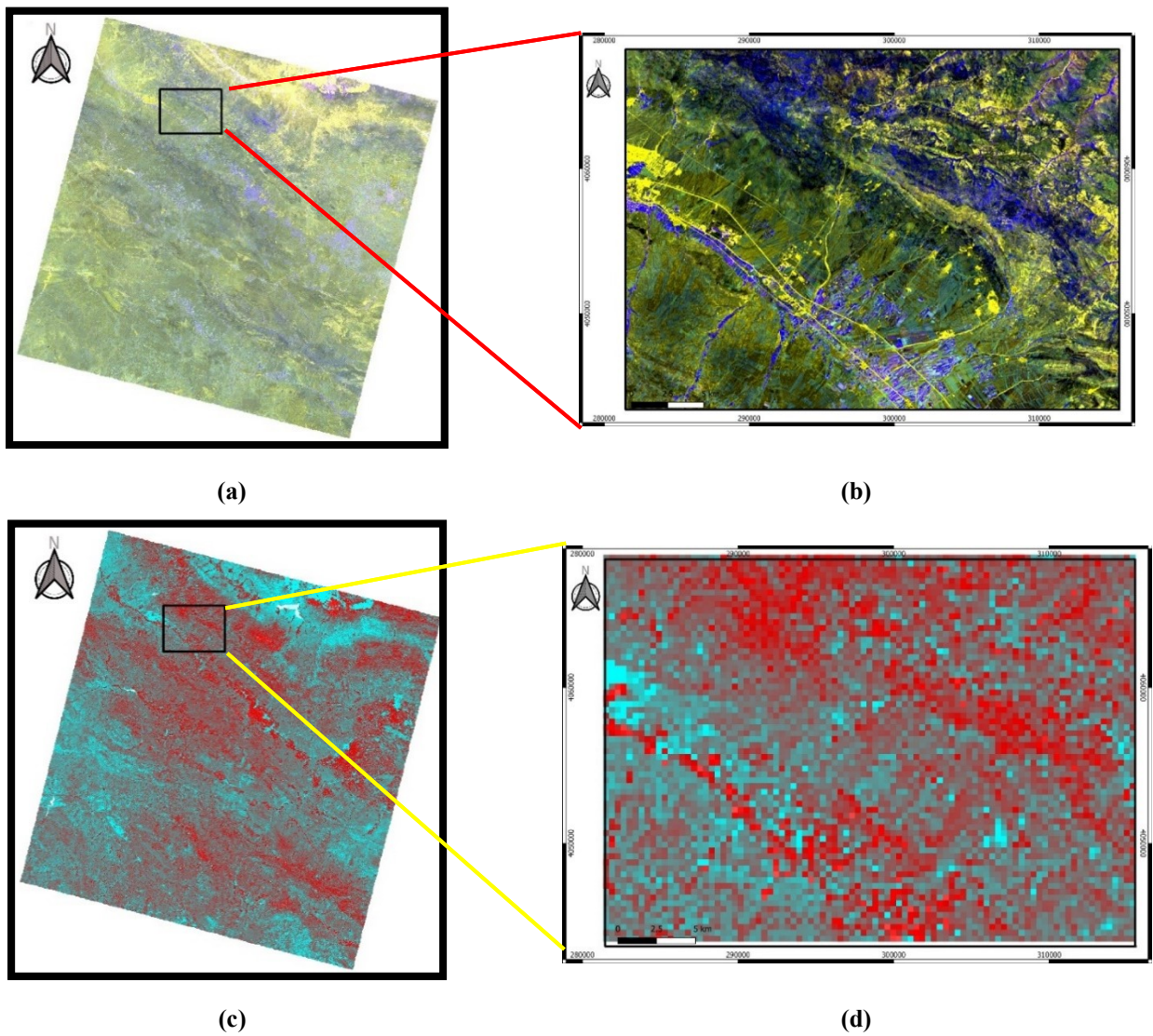


Figure 6. A. Results of visual interpretation, RGB: (7/5,7/2,7/1); magnetite mineralization is yellow. B. Selected studied area of RGB: (7/5,7/2,7/1) C. Result of visualization interpretation, RGB: (4/2,1,1); D. Selected studied area of RGB: (4/2,1,1) classified using SAM in three classes.

3.4. Spectral Angle Mapper (SAM)

This method was performed based on a similarity between the reference mineral spectrum and tested mineral spectrum for magnetite mineralization [34]. The similarity between the reference and pixel spectrums is evaluated via calculation of the angle between these spectra. The spectra are considered vectors in a multi-dimensional space. The angle between the reference reflectance and reflected spectrums of the pixel surface. It is represented as a measure of similarity. This method will be various from light effects, and will not be affected by the factors of sunlight because this angle among two vectors is independent from their length [34]. In an image achieved by the SAM method, each pixel shows the difference in reflection in the separation spectral pattern

reflected from the surface with the reference pattern. This difference in spectral pattern is displayed angularly and on a radian scale, between 0 and $\pi/2$ [35]. The output of SAM is a lighter pixel equivalent to a larger angle, indicating a greater difference between the studied and reference spectrums, and a darker pixel equivalent to a smaller angle and a symbol of greater spectrum similarity. However, the negative threshold for conversion was used to apply the display. Therefore, the output image will be an external image with the exposure of magnetite iron oxide (Figure 6). Then the calculated values of differences frequency angel between reference spectrum frequency of iron oxides and magnetite mineralization in the local area and processed remote sensing data, the values classified using Machin learning algorithm,

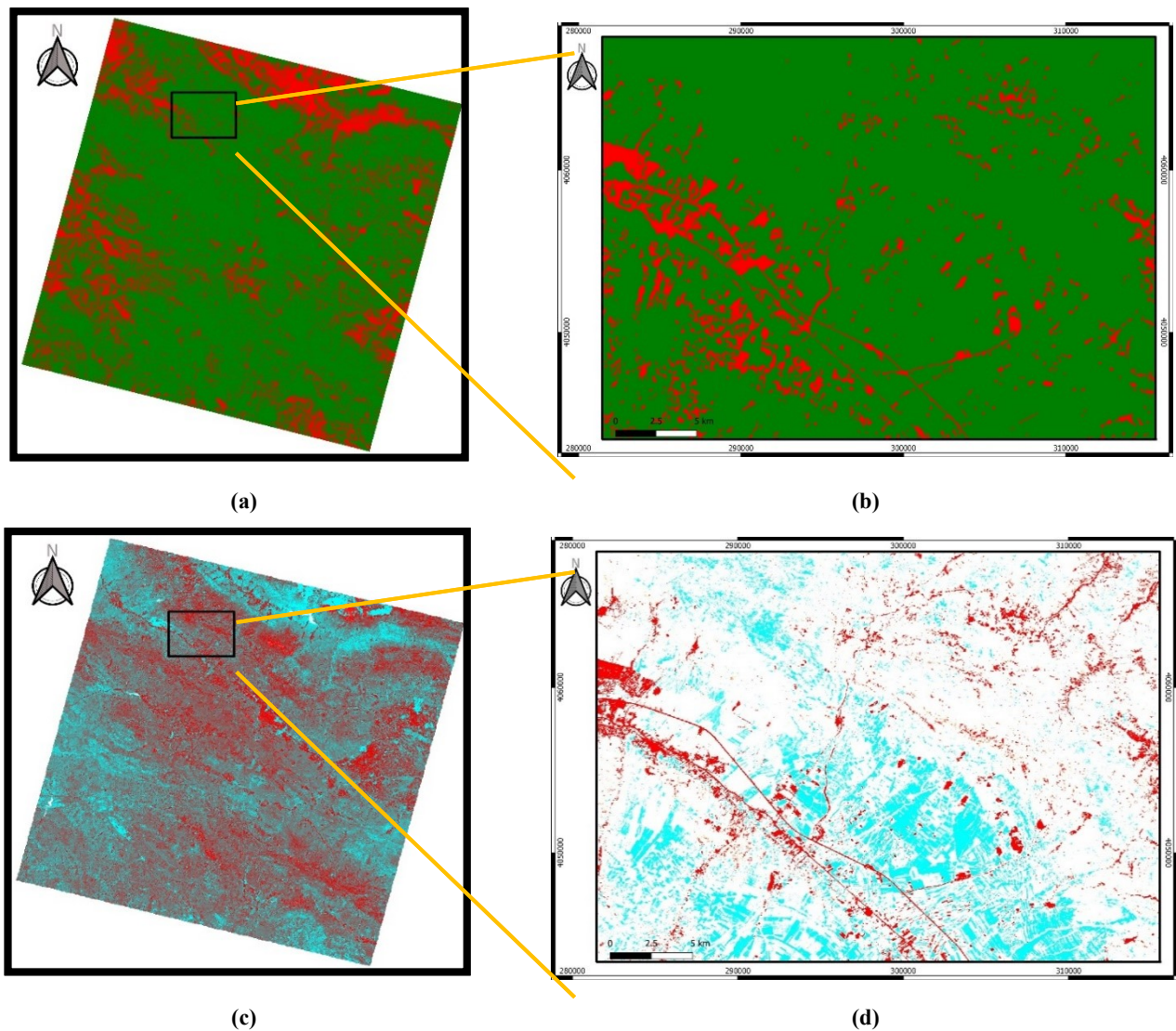


Figure 7. A. Magnetite mineralization map in two classes using SAM, target spectrum angel value, and others. B. Selected studied area of SAM C. Result of visualization interpretation, RGB: (4/2,1,1); D. Selected studied area of RGB: (4/2,1,1) classified using SAM.

3.5. NDVI and NDWI

NDWI is a remote sensing-based indicator sensitive to the change in the water content of leaves [36]. NDWI is computed using the near-infrared (NIR) and the short-wave infrared (SWIR) reflectances. In Landsat 8 the NIR band is band 5 (0.85-0.88 μm) and SWIR band is band 6 (1.57–1.65 μm).

The Normalized Difference Vegetation Index (NDVI) is a standard band-ratio calculation frequently used to analyze vegetation land cover using remote sensing data. NDVI is calculated from the ratio of the difference between NIR and the Red band, divided by the sum of them [37]. In Landsat 8, the NIR band is band 5 (0.85-0.88 μm) and the red band is band 4 (0.64-0.67 μm).

3.6. K-mean

This is one of the unsupervised classification algorithms, also called clusterization, that groups object into k groups based on their characteristics. This grouping was carried out by minimizing the summation of the distances between each object and the group or cluster centroid. The distance usually used is the quadratic or Euclidean distance.

Let $X = \{x_i\}$, $i = 1, \dots, n$ be the set of n d-dimensional points to be clustered at a set of K clusters, $C = \{c_k, k = 1, \dots, K\}$. K-means algorithm finds a partition such that the squared error between the empirical mean of a cluster and points in this cluster is minimized. Let μ_k be the cluster's mean as c_k . The squared error between μ_k and the cluster points c_k is introduced as:

$$J(c_k) = \sum_{x_i \in c_k} \|x_i - \mu_k\|^2 \quad (1)$$

K-means aim to minimize the summation of squared error over all K clusters,

$$J(C) = \sum_{k=1}^k \sum_{x_i \in c_k} \|x_i - \mu_k\|^2 \quad (2)$$

Minimizing the objective function is identified to be an NP-hard problem (even for $K = 2$; [38]). Thus K-means can only converge to a local lowest value, even though a recent study has denoted with a large probability K-means could converge to the universal optimum while the clusters are properly divided [36]. K-means commences with a primary divider by K clusters and allocates patterns to clusters for reducing squared error. Since the squared error always decreases with an increase in

the number of clusters K (with $J(C) = 0$ when $K = n$), this can be minimized only for a fixed number of clusters. These K-means major steps are as follows [44]:

The first step is initialization. Once the group's number, k has been chosen, k centroids are established in a data space, for instance, choosing them randomly. The second stage is one object of this data is assigned to its adjacent centroid, and the third step is centroids update and Computing new cluster centers. The centroid position for each group is updated taking as the new centroid the average situation of these objects belonging to said group. Repeat the second and third steps until the centroids do not move, or move below a threshold distance in each step.

After computing the band ratio of band4/band2 related to the iron alterations in the Tarom area and pixel values of Normalized Difference Vegetation Index (NDVI), the output images were classified using k-means algorithm at four clusters and 1 iteration. The Iron oxide and NDVI classified maps using the k-means algorithm were presented in Figure 7.

3.7. Multifractal S-A model

The multifractal models are used in various applications of earth sciences to delineate the values in thresholds. Aramesh Asl 2015 identified alteration zones and major faults based on ETM+ multispectral data using multi-fractal modeling [29]. In other studies, Koohzadi *et al.* used FFT/IFFT in the signal processing and time series analysis for Li exploration performing the spectrum-area [45]. Afzal *et al.* 2013 applied a spectrum-area fractal model to identify geochemical anomalies based on soil data in Kahang porphyry-type Cu deposit [46].

In this study, the alteration classes were delineated based on the intensity of the Iron-oxide mineralization using the S-A method, and each class was presented as an eligible zone. For demonstrating the preceding method, the output of band combination and band ratio methods were taken from visualization process results. The S-A log-log plots represent variations of the alteration phases. S was calculated for distributions using 2D FFT by a MATLAB code. Logarithmic S and A values were created against each other (Figure 8). The log-log plots contain six populations for iron oxide alteration and magnetite mineralization.

The components with relatively lower values of S and higher frequencies, give larger slopes ($2/\beta > 1$) implying. Threshold values for iron oxide and

magnetite were determined from log-log S-A plots, (Figure 8).

Based on these threshold values, the filters were designed for the separation of alteration classes

populations. All output classified images are used as alternative layers in the decision-making system to calculate the final integrated map (Figure 9).

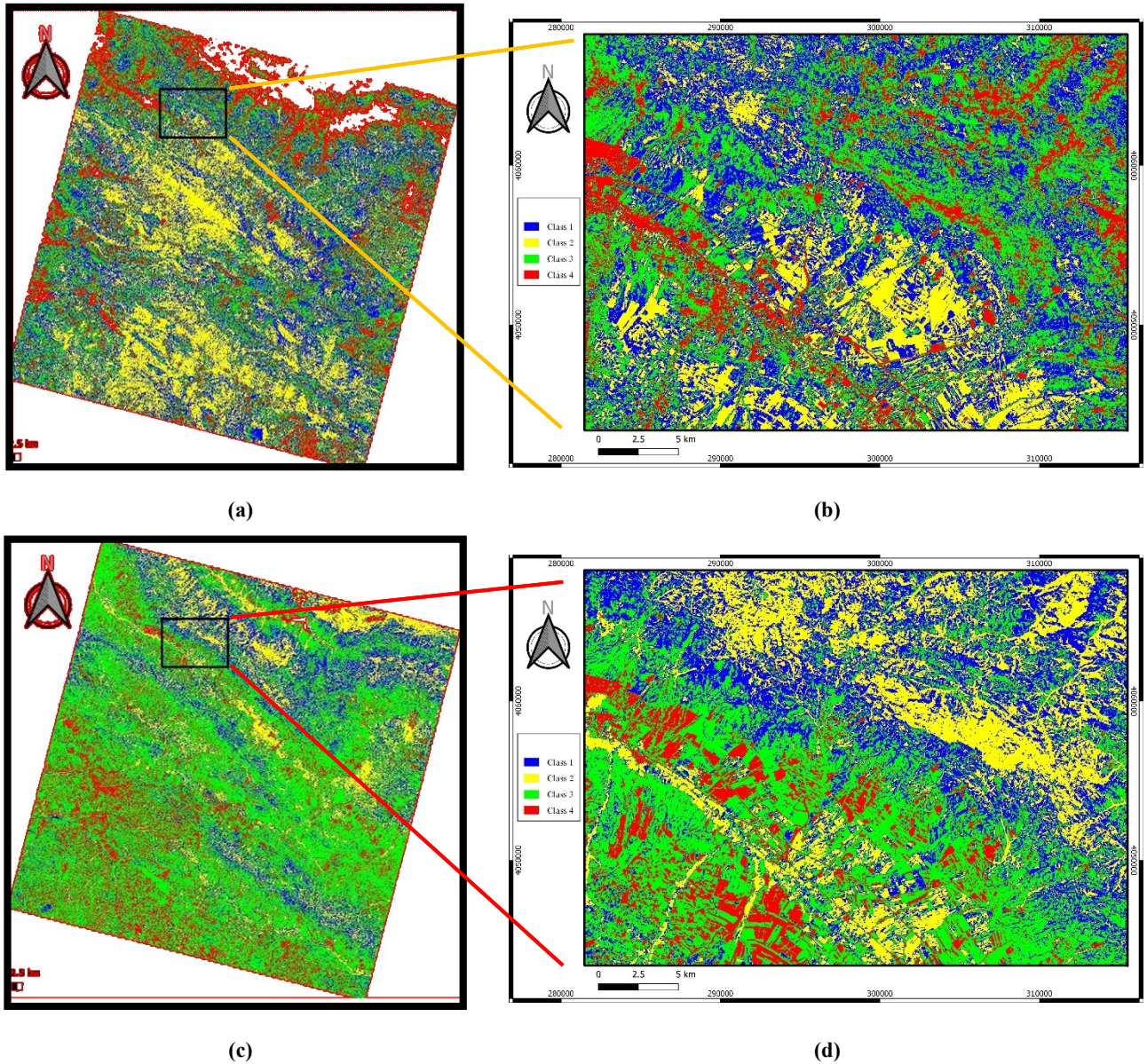
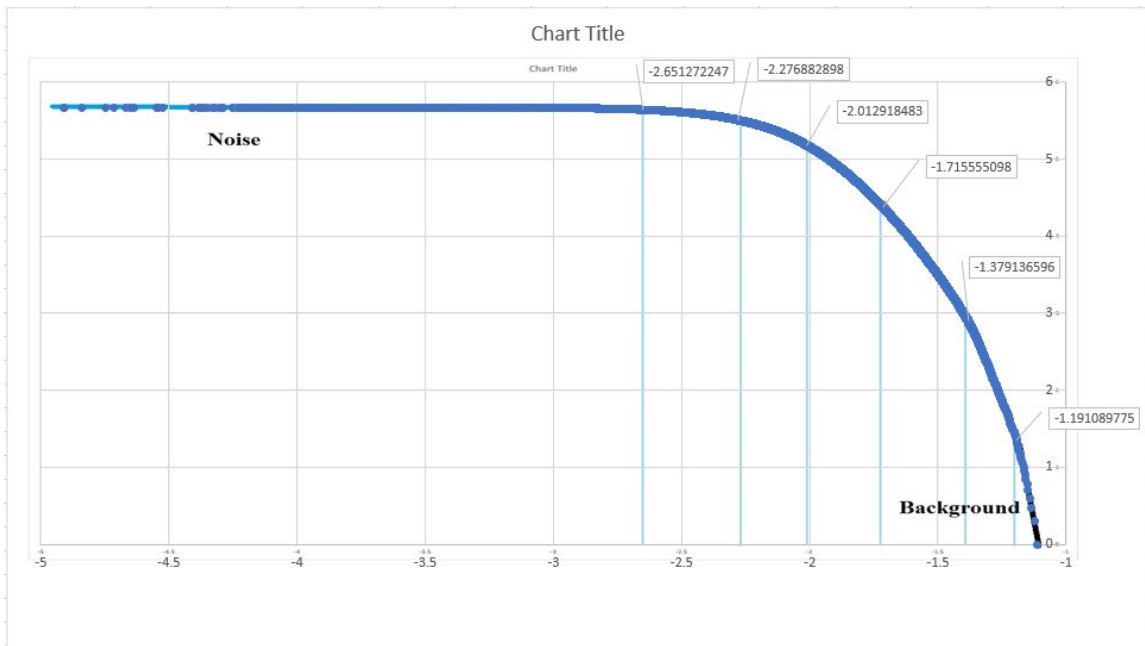
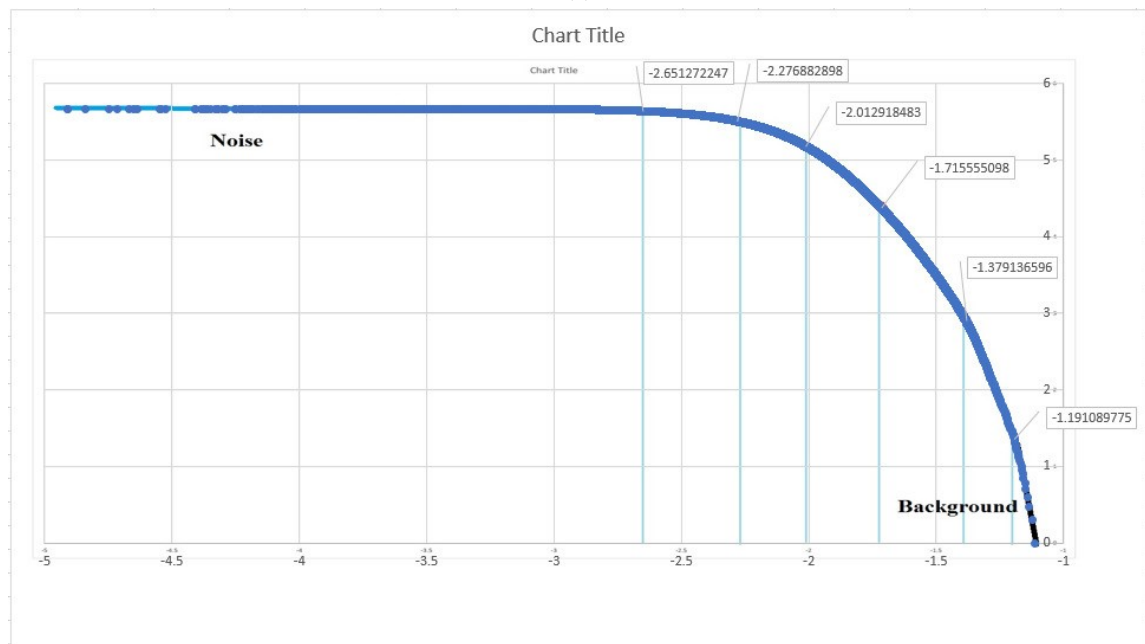


Figure 8. A. Classified map of Iron oxide using k-means in full scene. B. Classified map of Iron oxide using k-means in selected studied area in 4 classes. C. Classified map of NDVI using k-means in full scene. D. Classified map of NDVI using k-means in selected studied area in 4 classes.

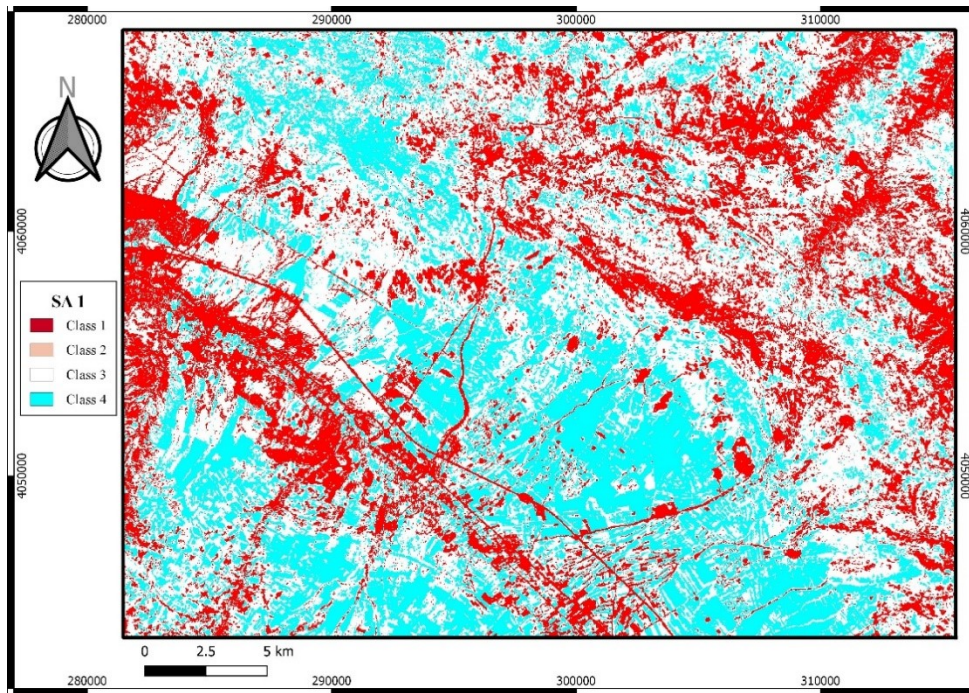


(a)

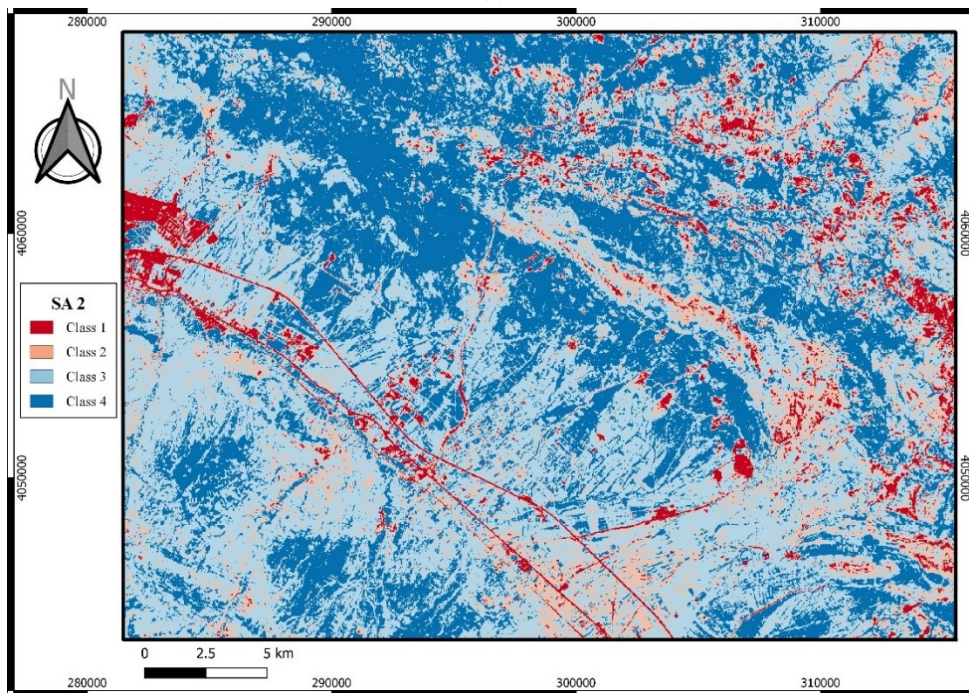


(b)

Figure 8. (A) S-A log-log plot iron oxide alteration in Tarom zone. (B) S-A log-log plot of magnetite iron oxide alteration zones in Tarom zone.

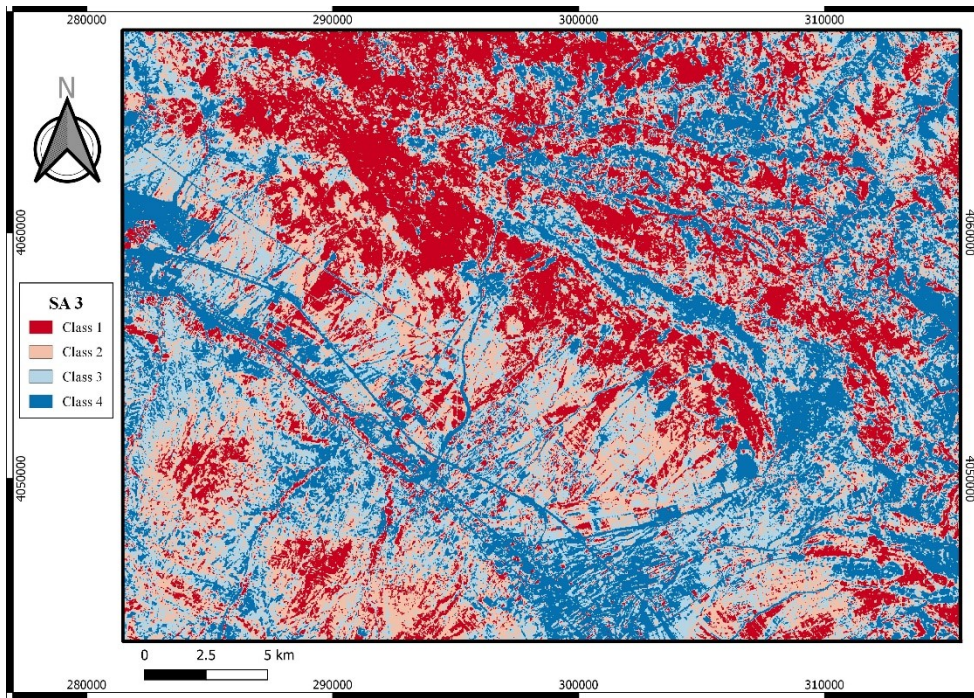


(a)

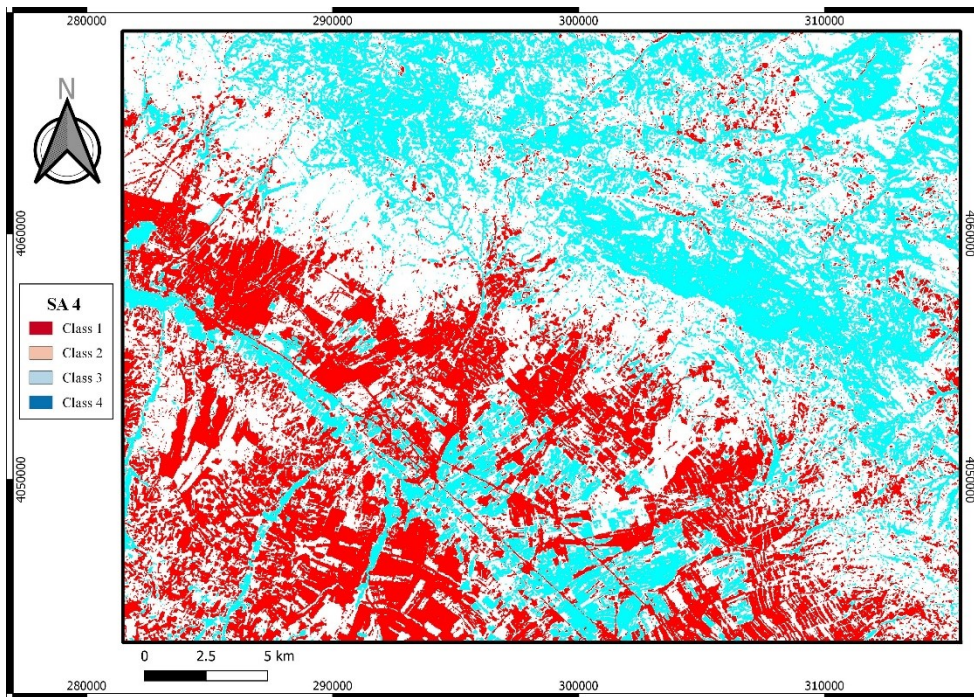


(b)

Figure 9. Classified maps using S-A algorithm.

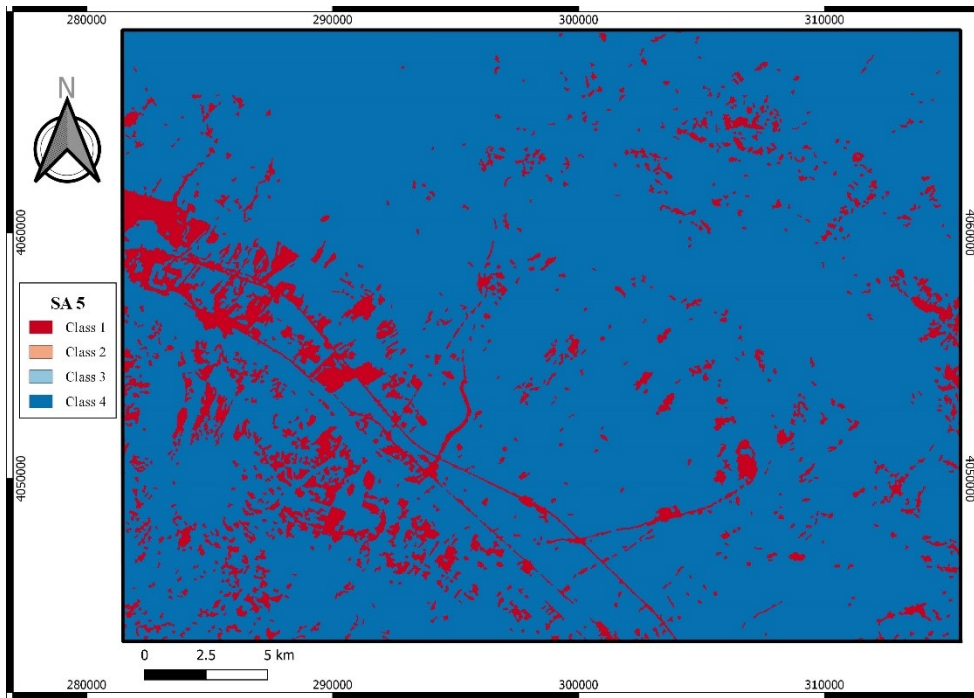


(c)

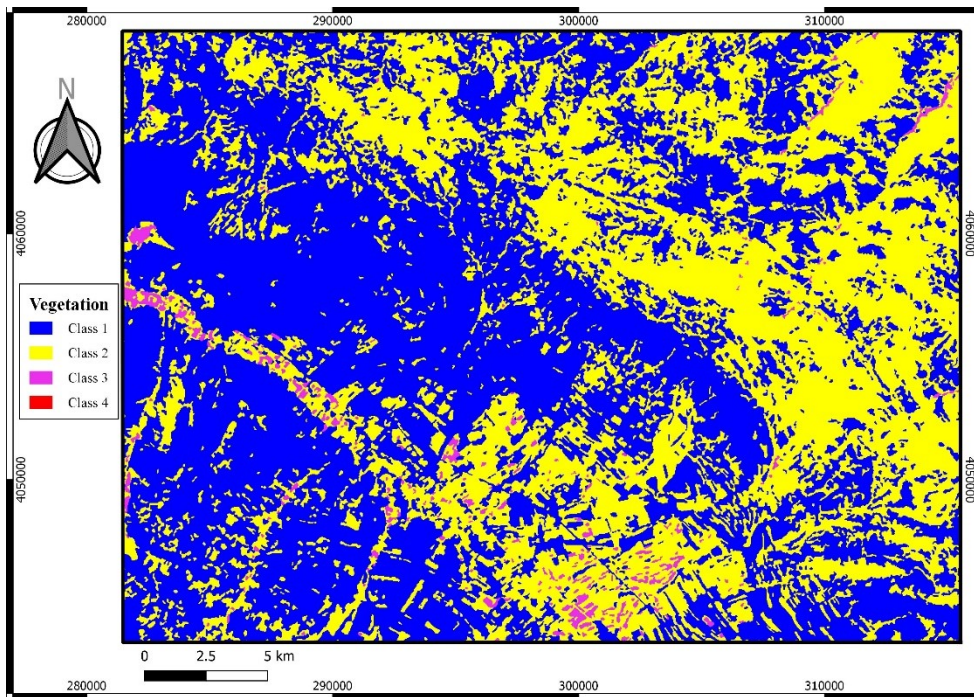


(d)

Continous of Figure 9. Classified maps using S-A algorithm.



(e)



(f)

Continuation of Figure 9. Classified maps using S-A algorithm.

3.8. MADM/MCDM

Multi-Attribute Decision Making (MADM) is a common task in human activities. It consists of finding the most preferred alternative from a given set. The layout strategy invariably has an important effect on the performance of a manufacturing or service industry system, and it has been an attractive research section now [47]. The previous method, e.g. Spiral [48] and Multiple, can

professionally create layout designs' alternatives but these objectives are often oversimplified. Consequently, numerous decision-making processes in real data occur in different group settings with incomplete information. Salo in 1995 established a collaborating technique to collect the group members' preferences in the context of an improving value representation [49]. Kim in 1999 presented a cooperating process for multiple

characteristic collection decision-making with insufficient information and described some theoretical models to establish a group’s pair-wise governance relationships by utility ranges with a distinguishable linear programming procedure [50]. Additional algorithmic approaches could be modeled the layout design problem as a mixed-integer programming formulation [51, 52]. Method for instruction performance by similarity to ideal solution (TOPSIS) was initially introduced by Hwang and Yoon in 1981 [53], and Lai *et al.* in 1994 [54], is a multi-attribute or multi-criteria decision-making [55, 56] to recognize explanations from a finite’s alternatives set based on the minimum and maximum distances from an ideal point and a negative ideal point, respectively. Shih in 2008 has extracted incremental investigation to overcome ratio scales drawbacks in different MCDM approaches [57]. Shih *et al.* in 2007 have identified the TOPSIS advantages that represent the basis of expert choice; the best and worst alternatives accounts; the efficiency measurements of all alternatives on features [58]. Nowadays, TOPSIS has been successfully used in different sciences [59-61]. However, uncertain data may not be precisely determined since human judgments are often vague under insufficient information. Therefore, fuzzy values or interval values are usually collected in the measurement of the relative importance of criteria and the performance of each alternative on the TOPSIS model [62]. Grobelny in 1987 has used a fuzzy approach to solve layout problems by a fuzzy method to describe the closeness association among sections and optimum design in the final stage [63]. A layout design problem using the MADM procedures is preferable. Multiple objective decision-making (MODM) as a programming technique includes a conflicting goal’s set that cannot be accomplished at the same time [64, 65].

3.9. TOPSIS

The method of “Technique for Order of Preference by Similarity to Ideal Solution” was proposed by Huang and Yoon in 1981, which was used by various researchers and users. In this method, the alternatives are ranked on the basis of similarity to the ideal answer [53]. There are two concepts of ideal solution and similarities to this. An ideal solution, as its name implies, is the solution that is the best in every way, which generally does not exist in practice, and it tries to get closer to it. For measurement of the similarity of an alternative to an ideal and counter-ideal

solution, the difference between the alternative and ideal and also the counter-ideal solution is measured. The alternatives are then evaluated and ranked based on the distance from the counter-ideal solution to the total distance from the ideal and counter-ideal solution. The TOPSIS technique has a strong mathematical backing, and like many scientific methods, the knowledge and observance of assumptions, the scope and conditions of validity of laws and the correctness of proposed formulas, and the accuracy of these results are very important. The TOPSIS process is a method with several very strong compensatory criteria/attributes for prioritizing alternatives by simulating the ideal answer. The steps to do this are as follows:

The results via the band composition, color combination, SAM, and SA methods were considered as selection alternatives that are input to the TOPSIS model decision matrix. Correspondingly, the output of bandwidth methods and bandwidth ratios optimized by the area power spectrum method were considered as two input alternatives SA1 and SA2 as input in the decision model. In order to minimize expert involvement in weighting and decision-making, and to minimize imposed calculations from other hierarchical methods, the TOPSIS method, which is according to the variation from the ideal and anti-ideal answers, was used. Bachelor-approved criteria include positive criteria for proximity to the target range of reference minerals (from the USGS Spectral Library), proximity to the proven terrestrial range, and negative criteria such as vegetation and agricultural land (NDVI), water, and moisture (Normalized Difference Water Index; NWDI), were abnormal effects and ways.

Step one:

Given the number of alternatives, criteria and the calculation of all alternatives for different criteria form a decision matrix. This decision matrix is formed as follows:

$$X = \begin{bmatrix} x_{11} & \dots & x_{1n} \\ \cdot & \dots & \cdot \\ \cdot & \dots & \cdot \\ \cdot & \dots & \cdot \\ x_{m1} & \dots & x_{mn} \end{bmatrix} \quad (4)$$

x_{ij} is the function of the i ($i = 1, 2, \dots, 6$) related to the criteria j ($j = 1, 2, \dots, 5$)

In this step, based on the available data, the final outputs of all methods were prepared by the expert as decision alternatives, that choice the best pixel

value related to the mineralization at that point (PIXEL).

In this research work, the alternatives are the output classes of SA1, ..., SA5, and k-means algorithm for ban4/band2 ratio. The NWDI, NDVI classified using k-means and Urban factors are negative criteria for alternatives, And closeness to Reference, spectral particulars of magnetite, closeness to reference spectral features of iron oxide are positive criteria for alternatives.

Step two:

The normalized decision matrix is calculated in this phase. Some normalized methods for TOPSIS are summarized by Shih *et al.* in 2008 [57]. To simplify, a vector normalization method is introduced whose normalized value r_{ij} is calculated as:

$$r_{ij} = \frac{x_{ij}}{\sqrt{\sum_{i=1}^m x_{ij}^2}} \quad (5) [57 \& 66]$$

r_{ij} is the normalized members of the decision matrix.

Step three:

In this step, the weighted normalized decision matrix is estimated. In order to importance of the attributes coefficient, the attributes weighting vector defines as follows:

$$W = [w_1 \ w_2 \ \dots \ w_n] \quad (6) [66]$$

At this stage, the criteria were given expert weight due to the expert opinion, field studies, and experiences of field experts.

Step four:

Calculating the weighted normalized decision matrix was carried out in this step. This matrix is given by multiplying this matrix by the attributes weighting vector:

$$v_{ij} = w_j \quad (7) [66]$$

$$j = 1, \dots, n$$

$$i = 1, \dots, m$$

Step five:

Determine A^+ as positive ideal and A^- negative ideal solution as below:

$$A^+ = \{v_1^+, v_2^+, \dots, v_j^+, \dots, v_n^+\} \quad (8)$$

$$A^- = \{v_1^-, v_2^-, \dots, v_j^-, \dots, v_n^-\} \quad (9) [66]$$

where v_j^+ is the best value of attribute j among all alternatives and v_j^- is the worst value of j among all the alternatives. The alternatives in A^+ and A^- represent completely better and completely worse alternatives, respectively. The result for measurements of the ideal and negative ideal solutions are indicated in Table 4.

Table 4. Result for ideal and negative ideal solution for criteria/attributes.

Solution	Urban factor	Closeness to reference spectral characteristics of magnetite	Closeness to reference spectral characteristics of hematite	NWDI and NDVI
Ideal	0.173	0.080	0.160	0.079
Negative ideal	0.087	0.0126	0.112	0.133

Step six:

In this step, for each alternative, the distances from the ideal and the negative ideal solutions are calculated from the following equations, respectively: index j represents the desired criterion, and index I represent the desired alternative (Table 5):

$$S_i^+ = \sqrt{\sum_{j=1}^n (v_{ij} - v_j^+)^2} \quad (10) [66] 0$$

$$S_i^- = \sqrt{\sum_{j=1}^n (v_{ij} - v_j^-)^2} \quad (11) [66]$$

Table 5. Each alternative distances from negative ideal and ideal solutions.

Alternative's index	1	2	3	4	5	6
Distance from ideal solution	0.070	0.052	0.050	0.061	0.076	0.098
Distance from negative ideal solution	0.070	0.064	0.066	0.082	0.082	0.098

Step seven:

Finally, the relative closeness of alternatives to the ideal solution are calculated. The relative closeness of any alternative A_i regarding A^+ is represented in the following form:

$$C_i^+ = \frac{S_i^-}{S_i^- + S_i^+} \tag{12} [66]$$

The similarity index varies between 0 and 1. If the closer alternative is to the ideal, then the similarity index value will be to one (Table 6).

Table 6. Value of similarity for alternatives.

Alternative pixel index	1	2	3	4	5	6
Similarity index or weighted	0.579	0.610	0.622	0.522	0.458	0.421

Step eight:

Rank preference order is carried out in this step. Choose an alternative with maximum C_i^+ or rank alternatives based on C_i^+ in descending order.

4. Results and Discussion

4.1. Integration

Mapping the integration of the image results of each process method needs to be standardized or stacked to be utilized as an alternative in the decision TOPSIS model. Pixel values of each image should be paired with other image pixels. In this work, the pixels without pair values participated in zones made by fair classification methods. The S-A method classified the processed images and made input alternatives for TOPSIS, although the decision calculations can reduce by new classes as new zones. The standard values are used for other pixels. The processing algorithm was performed (Figure 10).

4.2. Validation

The integrated map from all processed images and results show the target area of iron alterations. The final promising area map is validated by the mines/deposits and index layer shown in Figure 11. The final potential map shows a large correlation between iron oxide mineralization and existing indices and mines like magnetite mineralization in this region (Figure 11). However, the final potential map shows a large relationship between iron oxide and the target geological units based on the 1:100,000 geological map of Tarom. Alternations with more intensity are mostly located on the southern part of Tarom mountain range, and related to the Quartz-monzodiorite as qm unit (Figure 12) around Sorkheh Dizadj, Aliabad, Morvarid mines and around Zaker, Golestanabad and Zarnan deposits.



Figure 9. Flowchart of processing algorithm in this work.

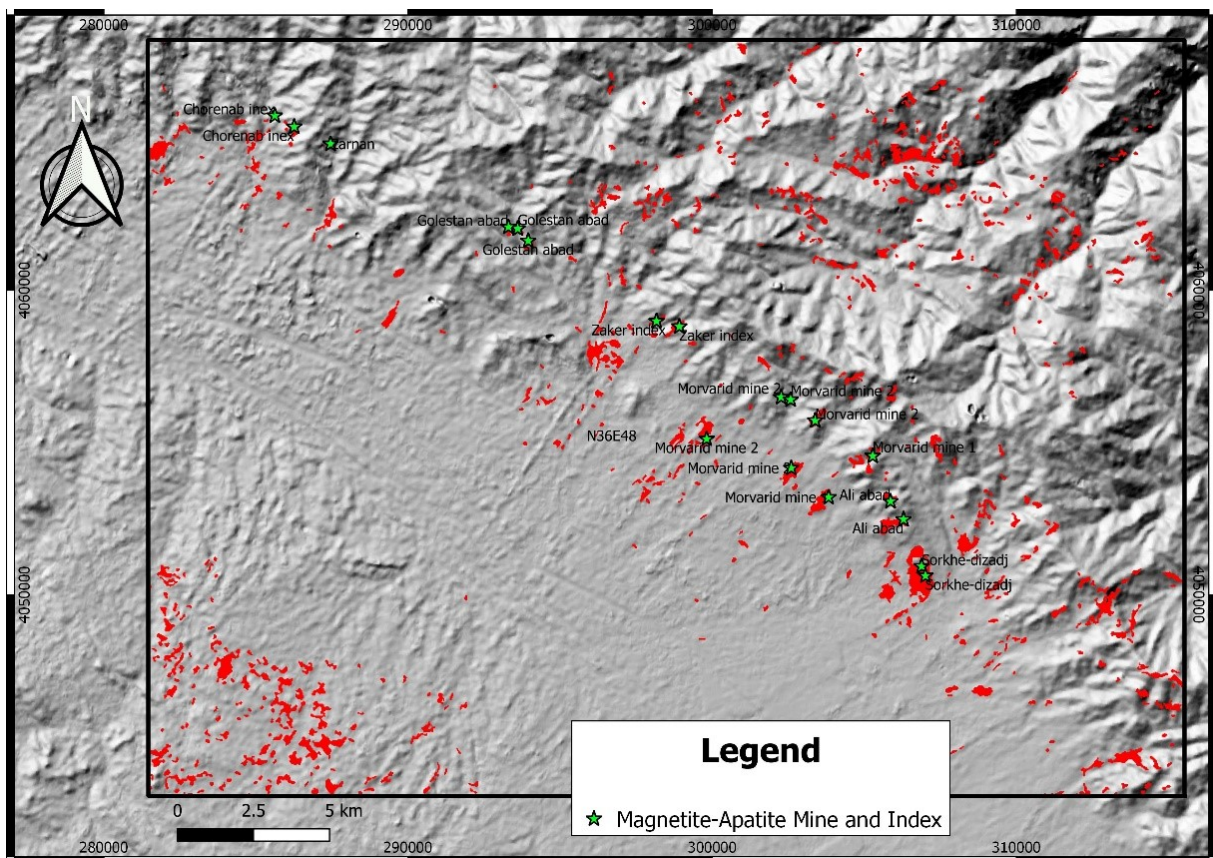


Figure 10. Integrated target map of iron oxide alteration in the Tarom studied area overlaid by mines/deposits and Index.

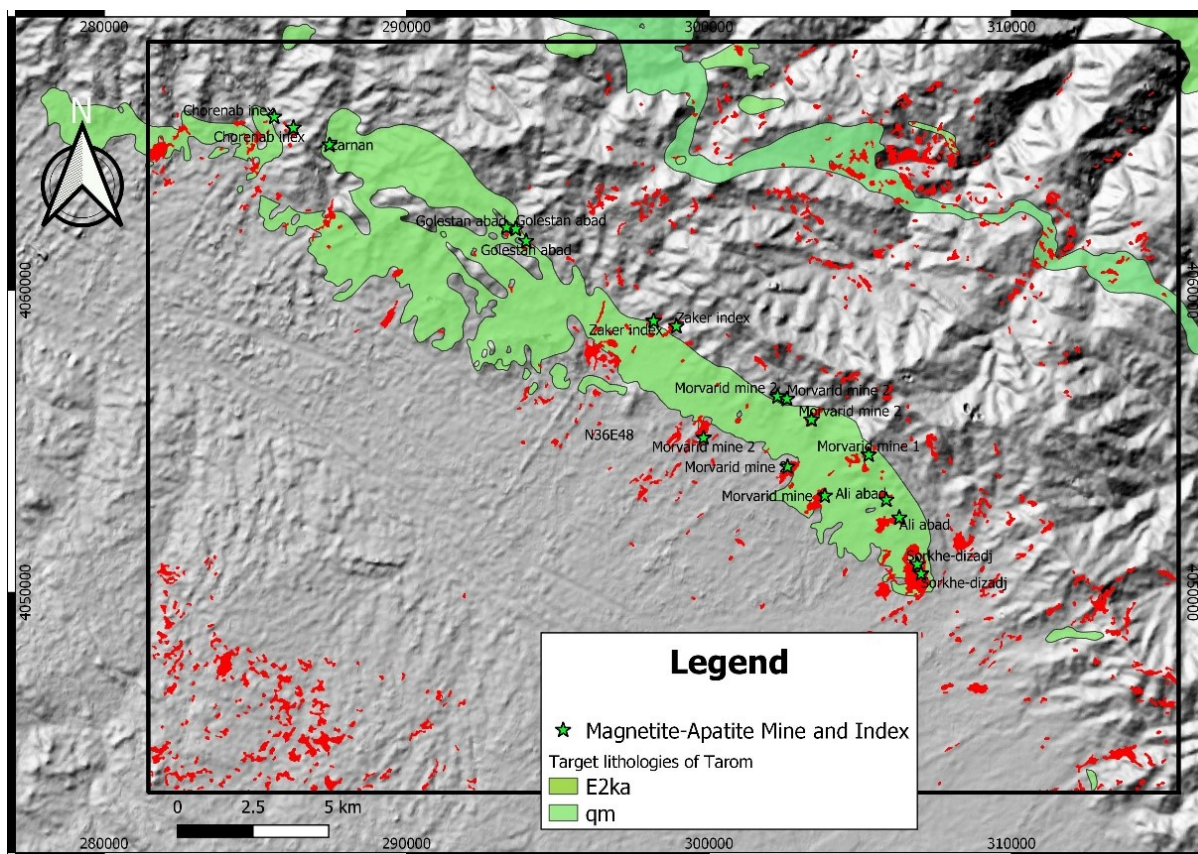


Figure 11. The integrated target map of iron oxide alteration in studied area overlaid by target lithologies from 1:100000 geological map of Taron (qm: Quartz-monzodiorite).

5. Conclusions

The iron alteration zones were identified on the Landsat8 OLI images by the methods of bond ratio, color combination, SAM, and S-A fractal model. The usage algorithm as a hybrid of the S-A fractal model and TOPSIS, which was applied by detecting alterations and increasing the accuracy of determining alteration zones by combining several criteria of different methods, could be applied to identify iron-magnetite deposits, which usually contain secondary oxide minerals, and iron hydroxides are at the level of indicator alterations, be very useful. The alteration zones can also be utilized as labeling classes in exploratory iron-apatite and magnetite-apatite exploration models on a semi-detailed scaling scale.

The results obtained by pixel value were closed either using the raw value of pixels (pixel-based method), then reclass the final results or reclass each alternative pixel for TOPSIS decision and apply the weight to final values (zone-based method). The pixel-based method shows a more accuracy in the final results but the zone-based method reduced the calculation processes. A combination of these methods is recommended according to the classes' variations.

References

- [1]. Sabins, F.F. (1999). Remote Sensing for Mineral Exploration. *Ore Geology Reviews*. 14, 157-183.
- [2]. Zhang, X, Pazner M, and Duke N. (2007). Lithologic and Mineral Information Extraction for Gold Exploration using ASTER Data in the South Chocolate Mountains (California). *ISPRS Journal of Photogrammetry and Remote Sensing*. 62, 271-282.
- [3]. Beiranvand Pour, A. and Hashim, M. (2012). The application of ASTER remote sensing data to porphyry copper and epithermal gold deposits. *Ore Geology Reviews*. 44, 1-9.
- [4]. Aramesh Asl, R., Afzal, P., Adib, A., and Yasrebi, A.B. (2015). Application of multifractal modeling for the identification of alteration zones and major faults based on ETM+ multispectral data. *Arab J Geosci.*; 8, 2997–3006.
- [5]. Yazdi, Z., Jafari Rad, A., Aghazadeh, M., and Afzal, P. (2018). Alteration Mapping for Porphyry Copper Exploration Using ASTER and QuickBird Multispectral Images, Sonajeel Prospect, NW Iran. *Journal of the Indian Society of Remote Sensing*. 46 (10), 1581–1593.
- [6]. Fakhari, S., Jafarirad, A., Afzal, P., and Lotfi, M. (2019). Delineation of hydrothermal alteration Zones for porphyry systems utilizing ASTER data in Jebal

- barez area, SE Iran. *Iranian Journal of Earth Sciences*. 11, 80-92.
- [7]. Zamyad, M., Afzal, P., Pourkermani, M., Nouri, R., and Jafari, M.R. (2019). Determination of Hydrothermal Alteration Zones by Remote Sensing Methods in Tirka Area, Toroud, NE Iran. *Journal of the Indian Society of Remote Sensing*. 47, 1817–1830.
- [8]. Sadeghi, B., Khalajmasoumi, M., Afzal, P., Moarefvand, P., Yasrebi, A.B., Wetherelt, A., Foster, P., and Ziazarifi, A., 2013 'Using ETM+ and ASTER sensors to identify iron occurrences in the Esfordi 1:100000 mapping sheet of Central Iran', *Journal of African Earth Sciences*, vol. 85, September 2013, pp. 103–114.
- [9]. Sadeghi, B., Khalajmasoumi, M., Moarefvand, P., and Afzal, P., 2012 'Extraction of iron alterations from ASTER SWIR and ETM+ data from Esfordi 1:100000 sheet (Central Iran)', *International Mining Congress & Expo*, Tehran, Iran.
- [10]. Rahimzadegan, M. and Sadeghi, B., 2016 'Development of the iterative edge detection method applied on blurred satellite images: state of the art', *Journal of Applied Remote Sensing*, Vol. 10 (3) 035018 doi: 10.1117/1.JRS.10.035018.
- [11]. Rahimzadegan, M., Sadeghi, B., Masoumi, M., and Taghizadeh Ghalehjoghi, S. 2015 'Application of target detection algorithms to identification of iron oxides using ASTER images: a case study in the North of Semnan province, Iran', *Arabian Journal of Geosciences*, Vol. 8, issue 9, pp. 7321–7331.
- [12]. Babaei, K. and Sadeghi, B., 2010 'Discrimination of alteration zones from ASTER SWIR data in the lead and zinc abandoned area of RoknAbad in Ardabil province', *International Mining Congress & Expo*, Tehran, Iran.
- [13]. Shamseddin Meigoony, M., Afzal, P., Gholinejad, M., and Sadeghi, B., 2012 'Processing and Comparison of Airborne Magnetic and ETM+ Data for Identification of Alteration Zones, Sarajeh 1:100000 Sheet, Qom', *Journal of Exploration Geology*, 5th year | 4th issue, pp. 31–43.
- [14]. Stocklin, J. (1968). *Structural History and Tectonic of Iran: A Review*. American Association of Petroleum Geologists Bulletin, USA, 52, 1229-1258.
- [15]. Nabatian, Gh. and Ghaderi, M. (2013). Oxygen isotope and fluid inclusion study of the Sorkheh-Dizaj iron oxideapatite deposit, NW Iran. *International Geology Review*. 55(4), 397-410.
- [16]. Nabatian, Gh., Ghaderi, M., Corfu, F., Neubauer, F., Bernroider, M., Prokofiev, V., and Honarmand, M., (2014). Geology, alteration, age and origin of iron oxide-apatite deposits in Upper Eocene quartz monzonite, Zanjan district, NW Iran. *Mineralium Deposita*, 49, 217–234.
- [17]. Khanmohamadi, N., Khakzad, A., and Izadyar, J. (2010). Mineralogy texture and genesis of Zaker iron-apatite deposit (NE Zanjan). *Scientific Quarterly Journal, Geosciences*. 76, 119-126 (in Persian with English abstract).
- [18]. Nabatian, Gh., Ghaderi, M., Daliran, F., and Rashidnejhad Omran, N. (2012). Sorkheh-Dizaj Iron Oxide-Apatite Ore Deposit in the Cenozoic Alborz-Azərbayjan Magmatic Belt, NW Iran. *Resource Geology*. 63 (1), 42–56.
- [19]. Nabatian, Gh., Ghaderi, M., Neubauer, F., Honarmand, M., Liu, X., Dong, Y., Jiang, S.Y., Von Quadt, A., and Bernroider, M. (2014). Petrogenesis of Tarom high-potassic granitoids in the Alborz Azarbaijan belt, Iran: Geochemical, U–Pb zircon and Sr–Nd–Pb isotopic constraints. *Lithos*. 184-187, 324- 345.
- [20]. U.S. Geological Survey. (2015. 2016). Landsat—Earth observation satellites (Ver. 1.2, April 2020). U.S. Geological Survey Fact Sheet. 3081, 4 p. (USGS-EROS; <http://earthexplorer.usgs.gov>).
- [21]. Hewson, R.D., Cudahy, T.J., Mizujiko, S., Ueda, K., and Mauger, A. L. (2005). Seamless geological map generation using ASTER in the Broken Hill-Currumona province of Australia. *Remote Sensing of Environment*. 99,159-172.
- [22]. Kumar, C., Shetty, A., Raval, S., Champati Ray, P.K., and Sharma, R. (2014). Sub-pixel mineral mapping using EO-1 Hyperion hyperspectral data. *International Archives of the Photogrammetry, Remote Sensing and Spatial Sciences*. XL-8, 455-461.
- [23]. Clark, R.N. (1999). Spectroscopy of Rocks and Minerals, and Principles of Spectroscopy, in: Rencz, A. (Ed.), *Manual of Remote Sensing*, Vol. 3. Wiley and Sons Inc., New York. pp. 3-58.
- [24]. Rowan, L., Hook, S.J., Abrams, M.J., and Mars, J.C. (2003). Mapping hydrothermally altered rocks at Cuprite, Nevada, using the Advanced Spaceborne thermal emission and reflection radiometer (ASTER), a new satellite-imaging system *Econ Geol Bull Soc Econ Geol*. 98 (5), 1019–1027.
- [25]. Yamaguchi, Y., Kahle, A.B., Kawakami, T., and Paniel, M., (1998). Overview of the advanced spaceborne thermal emission and reflection radiometer (ASTER). *IEEE Trans. Geosci. Remote Sens*. 36 (4), 1062–1071
- [26]. Han, T. and Nelson, J. (2015). Mapping hydrothermally altered rocks with Landsat 8 imagery: A case study in the KSM and Snow field zones, northwestern British Columbia. *British Columbia Geol. Surv*. 103–112.
- [27]. Mwaniki, M. W., Moeller, M. S., and Schellmann, G. (2015). A comparison of Landsat 8 (OLI) and Landsat 7 (ETM+) in mapping geology and visualising lineaments: a case study of central region Kenya *Int. Arch Photogramm. Remote Sens. Spat. Inf. Sci*. 40, 897.

- [28]. Van Der Meer, F. (2004). Analysis of spectral absorption features in hyperspectral imagery. *Int. J. Appl. Earth Obs. Geoinf.* 5, 55–68.
- [29]. Ali, A. S. and Beiranvand Pour, A. (2014). Lithological mapping and hydrothermal alteration using Landsat 8 data: a case study in ariab mining district, red sea hills, Sudan. *Int. J. Basic Appl. Sci.* 3, 199.
- [30]. Ducart, D. F., Silva, A. M., Toledo, C. L. B., and Assis, L. M. D. (2016). Mapping iron oxides with Landsat-8/OLI and EO-1/Hyperion imagery from the Serra Norte iron deposits in the Carajás Mineral Province, Brazil. *Braz. J. Geol.*; 46, 331–349.
- [31]. Prost, G. L. (2002). *Remote Sensing for Geologists: A Guide to Image Interpretation*, CRC Press. 2nd edn.
- [32]. Miyatake, S. (2002). Regional Lineament analysis and alteration mineral mapping for intrusive related copper exploration in the Myanmar central volcanic belt. *Proc. 23rd Asian Conf. on Remote Sensing*. pp. 1-4 (CD-ROM).
- [33]. Ren, D. and Abdelsalam, M. G. (2001). Optimum index factor (OIF) for ASTER data: examples from the Neoproterozoic Allaqi Suture, Egypt. *Proc. Geol. Soc. Am.* p. 123.
- [34]. Kruse F. A., Lefkoff A. B., Boardman J. B., Heidbrecht K. B., Shapiro A. T., Barloon P. J., Goetz A. F.H. (1993). The Spectral Image Processing System (SIPS) Interactive Visualization and Analysis of Imaging Spectrometer Data, *Remote Sensing of Environment*, Special issue on AVIRIS. V. 44, 145-163.
- [35]. Van der Meer F. and De Jong S. (2003). *Imaging Spectrometry. Basic Principles and Prospective Applications*, 4. Kluwer Academic Publishers, Dordrecht/ Boston/London. 35.
- [36]. Gao, B.-C. (1996). NDWI-A normalized difference water index for remote sensing of vegetation liquid water from space. *Remote Sensing of Environment*. 58: 257-266.
- [37]. Bannari, D. Morin, F. Bonn, and A. R. Huete. (1995). A review of vegetation indices, *Remote Sensing Reviews*. 13:1-2, 95-120.
- [38]. Drineas, P., Frieze, A., Kannan, R., Vempala, S., and Vinay V. (1999). Clustering large graphs via the singular value decomposition. *Machine Learn.* 56 (1-3), 9-33.
- [39]. Meila, Marina. (2006). The uniqueness of a good optimum for k-means. In: *Proc. 23rd Internat. Conf. Machine Learning*. pp. 625-632.
- [40]. Sadeghi, B. (2020) *Quantification of Uncertainty in Geochemical Anomalies in Mineral Exploration*. PhD thesis, University of New South Wales.
- [41]. Heidari, S.M., Afzal, P., Ghaderi, M., and Sadeghi, B. 2021 'Detection of mineralization stages using zonation and multifractal modeling based on geological and geochemical data in the Au-(Cu) intrusion-related Gouzal-Bolagh deposit, NW Iran', *Ore Geology Reviews*. (<https://doi.org/10.1016/j.oregeorev.2021.104561>).
- [42]. Sadeghi, B. 2021 'Simulated-multifractal models: a futuristic review of multifractal modeling in geochemical anomaly classification', *Ore Geology Reviews*. (<https://doi.org/10.1016/j.oregeorev.2021.104511>).
- [43]. Sadeghi, B. (2021) *Spectrum-Area Method*. In: Daya Sagar B., Cheng Q., McKinley J., Agterberg F. (eds) *Encyclopedia of Mathematical Geosciences*. *Encyclopedia of Earth Sciences Series*. Springer, Cham. https://doi.org/10.1007/978-3-030-26050-7_310-1
- [44]. Jain, Anil K., Dubes, Richard C. (1988). *Algorithms for Clustering Data*. Prentice Hall.
- [45]. Koohzadi, F., Afzal, P., Jahani, D., and Pourkermani, M. (2021). Geochemical exploration for Li in regional scale utilizing Staged Factor Analysis (SFA) and Spectrum-Area (S-A) fractal model in north central Iran. *Iranian Journal of Earth Sciences*. 13, 299-307.
- [46]. Afzal P, Harat H, Fadakar Alghalandis Y, and Yasrebi AB (2013) Application of spectrum–area fractal model to identify of geochemical anomalies based on soil data in Kahang porphyry-type Cu deposit, Iran. *Geochemistry* 73(4):533–543.
- [47]. Apple, J.M. (1991). *Plant layout and material handling*. Krieger.
- [48]. Goetschalckx, M. (1992). An interactive layout heuristic based on hexagonal adjacency graphs. *European Journal of Operational Research*. 63 (2), 304-321.
- [49]. Salo, A.A. (1995). Interactive decision aiding for group decision support. *European Journal of Operational Research*. 84 (1), 134-149.
- [50]. Kim, S.H., S.H. Choi, and J.K. Kim. (1999). An interactive procedure for multiple attribute group decision making with incomplete information: Range-based approach. *European Journal of Operational Research*. 118 (1), 139-152.
- [51]. Heragu, S.S. and A. Kusiak. (1991). Efficient models for the facility layout problem. *European Journal of Operational Research*. 53 (1), 1-13.
- [52]. Chan, F.T., K.W. Lau, P.L.Y. Chan, and K.L. Choy. (2006). Two-stage approach for machine-part grouping and cell layout problems. *Robotics and Computer-Integrated Manufacturing*. 22 (3), 217-238.
- [53]. Hwang, C.-L. and K. Yoon. (1981). *Multiple attribute decision-making*. Springer.

- [54]. Lai, Y.-J., T.-Y. Liu, and C.-L. Hwang. (1994). Topsis for MODM. *European Journal of Operational Research*. 76 (3), 486-500.
- [55]. Chen, S.-J.J., C.-L. Hwang, M.J. Beckmann, and W. Krelle. (1992). *Fuzzy multiple attribute decision making: Methods and Applications*, SpringerVerlag New York, Inc.
- [56]. Zeleny M. and J.L. Cochrane. (1973). *Multiple criteria decisions-making*. McGraw-Hill New York. Vol 25.
- [57]. Shih, H.-S. (2008). Incremental analysis for MCDM with an application to group TOPSIS. *European Journal of Operational Research*. 186 (2): 720-734 .
- [58]. Shih, H.-S., H.-J. Shyur, and E.S. Lee. (2007). An extension of TOPSIS for group decision-making. *Mathematical and Computer Modelling*. 45 (7): 801-813.
- [59]. Shyur, H.-J. and H.-S. Shih. (2006). A hybrid MCDM model for strategic vendor selection. *Mathematical and Computer Modelling*. 44 (7): 749-761 .
- [60]. Tzeng, G.-H., C.-W. Lin, and S. Opricovic. (2005). Multi-criteria analysis of alternative-fuel buses for public transportation. *Energy Policy*. 33 (11), 1373-1383 .
- [61]. Lin, M.-C., C.-C. Wang, M.-S. Chen, and C.A. Chang. (2008). Using AHP and TOPSIS approaches in customer-driven product design process. *Computers in Industry*. 59 (1), 17-31.
- [62]. Karray, F., E. Zaneldin, T. Hegazy, A.H. Shabeeb, and E. Elbeltagi. (2000). Tools of soft computing as applied to the problem of facilities layout planning. *Fuzzy Systems. IEEE Transactions*. 8 (4): 367-379.
- [63]. Grobelny, J. (1987). The fuzzy approach to facilities layout problems. *Fuzzy Sets and Systems*. 23 (2): 175-190.
- [64]. Yang, T. and C.-C. Hung. (2007). Multiple-attribute decision making methods for plant layout design problem. *Robotics and Computer-Integrated Manufacturing*. 23 (1): 126-137.
- [65]. Yang, T. and P. Chou. (2005). solving a multi-response simulation-optimization problem with discrete variables using a multiple-attribute decision-making method. *Mathematics and Computers in Simulation*. 68 (1): 9-21.
- [66]. Ataei M. *Multi-criteria decision making*. Shahrood: Shahrood university of technology; 2010.

تعیین محدوده‌های دگرسانی اکسید آهن با استفاده از مدل فرکتالی طیف توان-مساحت و روش تصمیم‌گیری تاپسیس در زون فلززایی طارم، زنجان

محمد مهدی پورغلام^۱، پیمان افضل^{۱*}، احمد ادیب^۱، کامبیز رهبر^۲ و مهران قلی‌نژاد^۱

۱- گروه مهندسی نفت و معدن، واحد تهران جنوب، دانشگاه آزاد اسلامی، تهران، ایران

۲- گروه مهندسی کامپیوتر، واحد تهران جنوب، دانشگاه آزاد اسلامی، تهران، ایران

ارسال ۲۰۲۲/۰۳/۲۲، پذیرش ۲۰۲۲/۰۶/۲۷

* نویسنده مسئول مکاتبات: P_Afzal@azad.ac.ir

چکیده:

روش‌های مبتنی بر آنالیز سیگنال از ابزارهای نیرومند و دارای استفاده گسترده در تحلیل داده‌های چندطیفی حاصل از دورسنجی هستند. هدف اصلی این نوشتار جدایش محدوده‌های دگرسانی اکسید آهن با استفاده از روش فرکتالی طیف توان-مساحت بر پایه داده‌های گرفته از ماهواره لندست ۸ OLI در زون فلززایی طارم واقع در استان زنجان می‌باشد. این محدوده‌های دگرسانی بصورت کلی براساس تغییرات شاخص نرمال شده آب و پوشش گیاهی و با استفاده از روش‌های نسبت و ترکیب باندی بارزسازی شده‌اند. سپس با استفاده از روش‌های سنجش زاویه طیفی، میانگین‌های کا و مدل‌سازی فرکتالی طیف توان-مساحت مورد دسته‌بندی قرار گرفته‌اند. محدوده‌های بدست آمده دارای همبستگی مثبت با کانه‌زایی‌های آهن موجود در منطقه بخصوص کانسارهای مگنتیتی بوده و در نهایت مناطق امیدبخش حاصله با استفاده از سیستم تصمیم‌گیری تاپسیس مورد رده‌بندی قرار گرفته‌اند.

کلمات کلیدی: روش فرکتالی طیف توان-مساحت، لندست ۸ OLI، تاپسیس، دگرسانی اکسید آهن، طارم.
